Published in final edited form as:

ACS Appl Mater Interfaces. 2017 March 01; 9(8): 6878–6884. doi:10.1021/acsami.6b15728.

Increasing binding efficiency via reporter shape and flux in a viral nanoparticle lateral-flow assay

Jinsu Kim[a], **Binh Vu**[a], **Katerina Kourentzi**[a], **Richard C. Willson**[*,a,b,c], and **Jacinta C. Conrad**[*,a]

[a]Department of Chemical & Biomolecular Engineering, University of Houston, Houston, Texas 77204, United States

[b]Department of Biology & Biochemistry, University of Houston, Houston, Texas 77204, United States

[c]Centro de Biotecnología FEMSA, Tecnologíco de Monterrey, Monterrey, Nuevo León, México

Abstract

To identify factors controlling the performance of reporter particles in a sensitive lateral-flow assay (LFA), we investigated the effect of the flux and shape of filamentous bacteriophage (phage) on the performance of phage LFAs. Phage of three different lengths and diameters were modified with biotin and AlexaFluor 555 as binding and read-out elements, respectively. The binding efficiencies of the functionalized phage were tested in a fibrous glass LFA membrane modified with avidin. The total binding rate, quantified using real-time particle counting and particle image velocimetry, decreased monotonically with the average bulk flux of phage through the membrane. At the pore scale more phage bound in regions with faster local flow, confirming that both average and local flux increased binding. The number of bound phage increased with the aspect ratio of the phage and scaled with the phage surface area, consistent with a binding interaction controlled by the number of recognition elements on the surface. Together, these results indicate that increasing the likelihood that recognition elements on the surface of phage encounter the fibers enhances the assay binding efficiency and suggests one origin for the improved performance of nonspherical phage reporters.

Graphical abstract

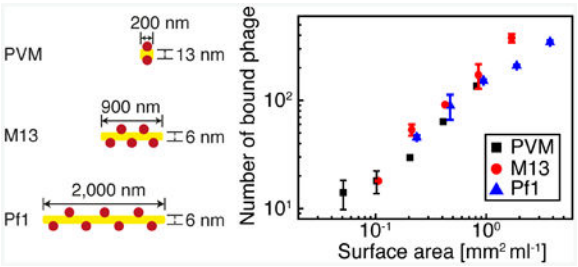

*Corresponding authors: willson@uh.edu, jcconrad@uh.edu.

Keywords

point-of-care diagnostic; lateral-flow; binding efficiency; anisotropic reporters; nanoparticle transport; viral nanoparticles

Introduction

Point-of-care (PoC) devices enable medical testing at the site of patient care and are becoming increasingly important.[1] The lateral-flow assay (LFA), one of the most widely used and commercially available PoC formats, is inexpensive, simple, portable, and rapid, and hence is well suited for testing in settings lacking complex laboratory equipment.[2] In a typical LFA format, analytes suspended in a fluid from a sample are dispensed onto one end of a test strip, typically a porous membrane. Capillary forces drive the fluid to flow along the strip; the analytes, entrained in the flowing fluid, are captured by antibody-coated reporters dried on an upstream conjugate pad. Capture antibodies at the test line recognize and capture the analyte-reporter complexes to produce a visual signal. Although traditional LFAs are widely employed to detect pregnancy and infection,[3] their use elsewhere is often limited by lack of analytical sensitivity and difficulties in quantification.[4] The performance of LFAs can be improved by tuning assay parameters, including fluid velocity,[5] reagent concentration,[6] and reporter particle size.[7] Increasing the analytical sensitivity of LFAs would expand their usefulness, including pathogen monitoring in food[8] and biopharmaceutical manufacturing.[9]

Research efforts towards developing sensitive and quantitative LFAs suitable for a broader range of applications have focused on new assay membranes,[5, 10-11] reporter materials,[12, 13] and read-out methods.[14, 15] In addition to assay materials, the affinity and kinetics of the antibodies used and readout modalities, the sensitivity of LFAs relies on the transport and binding of analytes and reporters to the sensing surface.[16] Binding effectiveness is measured by the number of binding events, which depends on the balance between the rate at which analytes encounter the sensing surface and the duration of their encounters with receptors there.[17] The rate at which targets encounter the sensing surface, therefore, is as critical as molecular binding kinetics in increasing the number of binding events. In many microfluidic-based sensors, targets are delivered to the sensing surface through convective and diffusive transport processes, for which Péclet (Pe) and Damköhler (Da) numbers can be calculated to identify the mechanisms that dominate transport and binding.[18-19] In reaction-limited conditions, the binding-reaction rate is much slower than the rate of transport to the surface (i.e. $Da \gg 1$), and hence analytes must encounter the surface for long times to bind.[20] Decreasing the flow rate can increase the encounter duration but does not necessarily increase total successful binding, as the rate at which targets encounter the sensing surface also decreases. To increase LFA sensitivity, there is a need to understand the effects of flow rate on the binding of analytes and reporters.

Most LFA reporters are spherical nanoparticles of gold, latex, carbon, or silver, which are inexpensive and are readily manufactured in a range of sizes.[21] Recent studies of adhesion of biological particles to surfaces, however, suggest that non-spherical nanoparticles may bind

more efficiently than spherical nanoparticles.[22] At least two mechanisms have been proposed to explain this increased surface binding efficiency. First, torques on non-spherical particles in shear flows can generate tumbling, rolling, or lateral drifting dynamics[23] that increase the rate of encounter with the surface. Second, a non-spherical particle has greater surface area and lower hydrodynamic drag than a sphere of the same volume.[24] These mechanisms would also be expected to affect binding of non-spherical LFA reporters. Indeed, a recent study showed that gold-coated silica nanorods used as reporters improved the sensitivity of an LFA for proteins by fifty-fold compared to spherical gold nanoparticles.[25] Surprisingly, the role of shape in LFA sensitivity has not yet been systematically explored – in part because many synthetic nanorods are very heterogeneous in both size and shape.[26]

In previous work, we developed functionalized M13 filamentous bacteriophage (phage) as an efficient, inexpensive, and biocompatible reporter for very sensitive LFAs.[27-29] M13 phage are filamentous viral nanoparticles (900 nm long and 6 nm diameter) that infect and replicate within *Escherichia coli*. Phage produced within *E. coli* are very uniform in size and shape, and can readily serve as a scaffold on which to attach multiple biorecognition and read-out-signal molecules. Recently, we showed that the flow field within an LFA membrane couples to the phage shape and promotes reorientation for binding, and hypothesized that binding efficiency can be increased by tuning the size and shape of reporters.[30]

In this paper, we show that the binding efficiency in an LFA is modulated by reporter shape and is coupled to flux. We used three filamentous phage of different sizes as model reporters in a simplified LFA. Phage were functionalized on their coat proteins with biotin, a recognition molecule, and AlexaFluor 555, a readout molecule. By imaging phage as they flowed through and bound to fibrous-silica LFA membranes modified with biotin-binding NeutrAvidin, we identified two mechanisms that increased the number of bound phage. First, the number of bound phage increased with phage length, and scaled with phage surface area and number of capsid proteins. Second, the number of bound phage increased with the average bulk flux, which in turn depended on the concentration of phage and the flow rate. Increasing either the phage flux or length increased the likelihood that phage encountered a fiber. Although phage predominantly bound at the onset of flow, when the bulk flow rate was fastest, at the local (pore) scale the flow rate varied both spatially and temporally. For a given average bulk flow rate, phage were more likely to bind in regions of the membrane featuring faster-than-average flows, again consistent with the idea that higher flux increased the probability of encounter with the membrane fibers. Finally, we examined the directionality of binding. Bound phage did not show a preferred orientation for binding, indicating that the angle at which phage approached fibers did not alter binding efficiency. The large number of biotins attached to the phage major coat proteins enabled multivalent binding and minimized any orientational dependence. Our results indicate that reporter length and flux are tunable design parameters that can be used to modify the binding efficiency in LFAs. More generally, we expect that these insights can be used to control micro- and nanoparticle capture in a variety of open porous media for a broad range of applications.

Materials and Methods

Biotinylation of phage

Asla Biotech generously provided wild type filamentous Pf1 bacteriophage (Pf1) and potato virus M virus-like particles[31] (PVM), and M13 bacteriophage (M13) was from the American Type Culture Collection (#34768). Phage were biotinylated on the primary amines of the major phage coat proteins using EZ-Link®Sulfo-NHS-LC-Biotin reagent (ThermoFisher Scientific, #21327), according to the manufacturer's instructions. We used 10^{12} molecules of biotin reagent to modify ~10^{10} phage, and removed excess biotin using a 7K MWCO Zeba spin desalting column (Thermo Scientific #89877).

AlexaFluor 555 labeling of phage (Fluor-phage)

Biotinylated Pf1, PVM, and M13 phage were further modified with AlexaFluor 555 Carboxylic Acid (Succinimidyl Ester, Life Technologies #A-20009) on their coat proteins as previously described.[28] Biotinylated Fluor-phage were detectable by epi-fluorescence microscopy and capturable by NeutrAvidin (Figure 1).

Confirmation of Fluor-phage biotinylation using enzyme-linked immunosorbent assay (ELISA)

100 μl of biotinylated Fluor-phage or control non-biotinylated Fluor-phage at concentrations of 0, 10^6, 10^7, 10^8 and 10^9 pfu ml^{-1} in 2% (w/v) BSA were added to NeutrAvidin-coated 96-well plates (Pierce Reacti-bind, Thermo Scientific #15128). After 2 h incubation at room temperature, the plate was rinsed four times each with PBST (PBS containing 0.05% (v/v) Tween 20) and PBS, respectively. Next, bound biotinylated Fluor-phage were allowed to react with 100 μl of horseradish peroxidase (HRP)-conjugated StreptAvidin (1:5,000 dilution, ThermoFisher Scientific, #N100) for 1 h at room temperature, then rinsed. 50 μl of TMB was added to the plate to develop the color for 15 min, and the reaction was terminated by adding 50 μl of 2 N H2SO4. Absorbance was measured at 450 nm in an ELISA reader (Tecan, Infinite M200 PRO).

Flow experiments

Fusion 5 LFA matrix strips (GE Healthcare & Life Sciences #8151–9915, with average pore diameter 8.9 ± 0.1 μm, average pore throat diameter 3.1 ± 0.1 μm, porosity 0.81 ± 0.01, and average fiber diameter $D = 4 \pm 2$ μm; cut into 3 mm × 50 mm × 0.35 mm strips) were modified with 3 μl of 1 mg ml^{-1} NeutrAvidin (Thermo Scientific, #3100) in 50 mM acetate buffer at pH 4.0 that was spotted at a fixed distance of 1 cm from the downstream end of the strip. After drying in air for 2 h at room temperature, each functionalized strip was placed on a large coverslip (48 × 65 mm, Gold Seal), covered with a second, smaller coverslip (22 × 22 mm, Fisher Brand), and placed on the stage of an epi-fluorescence microscope (Leica DMI 3000B) equipped with a 63× oil immersion objective lens (NA 1.4), as shown in Figure S-1. For model LFA experiments, biotinylated Fluor-phage were suspended in a background solution containing 0.1% (w/v) hydrolyzed polyacrylamide (HPAM, FLOPAAM 3330, SNF, weight-averaged molecular weight of 8 MDa) and 30% (v/v) glycerol in PBST (PBS containing 0.01% (v/v) Tween 20) to increase the fluid viscosity (and thereby reduce the

flow speed) and to nearly match the index of refraction of the fibers in the LFA strip, improving the image quality. Subsequently, 25 μl of 2-fold serially diluted phage at concentrations of $\frac{1}{2} \times 10^8$, $\frac{1}{4} \times 10^8$, $\frac{1}{8} \times 10^8$, $\frac{1}{16} \times 10^8$, and $\frac{1}{32} \times 10^8$ pfu ml^{-1} was dropped on the upstream end of the strip. Biotinylated Fluor-phage were imaged in capillary-driven transport through the membrane using a sCMOS camera (pco.edge 4.2, 30 frame sec^{-1}, 30 ms exposure time, 208.3 μm × 213 μm image field of view). The position of the fluid interface scaled as the square root of time,[30] following Washburn's equation.[32] Recording began immediately after liquid breakthrough in the field of view (t = 0 sec) and ceased when the phage particles exhibited only Brownian (rather than advective) motion, typically after six minutes. Three movies in different membranes were analyzed for each concentration and type of phage.

Counting of bound phage

In flow experiments, phage bound to fibers over time and accumulated in the images as static particles (Figure S-2a). To locate and count phage bound to fibers over time, we manually analyzed nine three-second intervals (starting at 20, 60, 100, 140, 180, 220, 260, 300, and 340 sec) in each of the three movies for a given phage and concentration and identified groups of bright pixels as bound phage. We set the position of each bound phage as its brightest pixel (Figure S-2b). This position differed by less than a pixel from the centroid position, calculated by weighting each pixel with its intensity; hence we obtained half-pixel accuracy.

Pre-image processing for particle image velocimetry (PIV)

We measured the local velocity at different positions in the field of view using PIV. Phage bound to the membrane generated a static background signal that impaired PIV processing. Hence prior to PIV processing we removed bound phage and other static background in the images. For each three-second movie we created a background image (Figure S-1c) that contained the minimum intensity at each pixel over time. This background was subtracted from each image in the movie (Figure S-2d).

PIV Analysis

To obtain the flow velocity profiles, PIV[33] was performed on the images in three-second movies of a sample containing M13 phage at a high concentration of $\frac{1}{2} \times 10^8$ pfu ml^{-1}. A high phage concentration improved statistical correlations and reduced error across the field of view of the image.[33] After pre-processing, we performed PIV[34] (JPIV software, downloaded from http://www.jpiv.vennemann-online.de/) using an interrogation window of 8 pixel × 8 pixel, a vector spacing of 3 pixel × 3 pixel, and a median filter of 3 pixel × 3 pixel. Four sequential images were correlated and averaged to generate PIV output at 20, 60, 100, 140, 180, 220, 260, 300, and 340 sec. From the flow vectors obtained from PIV, flow rates and directions were decoupled and represented as separated maps (Figure S-3).

Determination of flow direction on fiber surface

To locate the fibers, a brightfield micrograph of fibers was acquired in the same focal area as each flow movie. Because the intensity and transparency of fibers varied across each image (Figure S-4a, left), we segmented the fiber features from the background manually; fiber areas in the image were painted with black to generate extreme contrast, after which the threshold was applied to the painted image (Figure S4a, center). To obtain the fiber directions, each fiber segment was labeled using connected component labeling. Next, an axis-aligned bonding box was applied to the labeled fibers. The orientation of fibers was calculated (in degrees, relative to the +*x*-axis) from the length and width of the bounding box (Figure S-4a, right). Finally, the flow direction obtained from PIV was correlated with the fiber orientation. The range of relative angles between flow and fiber varied from 0° (parallel) to 90° (vertical). Four different formulas were used to calculate the relative angle, depending on the angular ranges of the fiber (ϕ) and flow (θ) directions (Figure S-4b).

Correlation of local flow with bound phage

The output from the PIV algorithms (Figure S-5a) provided both the magnitude and direction of flow at each location within the image. From this output, the local flow rate (Figure S-5d) and direction (Figure S-5e) were obtained for each position on a fiber (Figure S-5f) at which a phage bound.

Results and Discussion

Characterization of biotinylated Fluor-phage

Three filamentous phage of different dimensions (PVM, length 200 nm and width 13 nm; M13, length 900 nm and width 6 nm; and Pf1, length 2,000 nm and width 6 nm; Table 1) were functionalized with biotin and AlexaFluor 555. Fluorescence micrographs confirmed the successful fluor labeling of biotinylated phage (Figure 2). We assayed the biotinylation of the Fluor-phage via binding on NeutrAvidin-coated plates. Biotinylated Fluor-phage exhibited a positive signal whereas control non-biotinylated Fluor-M13 gave no significant signal (Figure S-6), confirming that only biotinylated Fluor-phage bound specifically to the NeutrAvidin-coated plate.

Comparison of number of bound phage PVM, M13 and Pf1 in LFA

To compare the binding efficiency of phage of different lengths in the Fusion 5 membrane, we counted the number of bound phage as a function of time and concentration ($\frac{1}{2} \times 10^8$, $\frac{1}{4} \times 10^8$, $\frac{1}{8} \times 10^8$, $\frac{1}{16} \times 10^8$, and $\frac{1}{32} \times 10^8$ pfu ml^{-1}), as shown in Figure 3a, b and c for PVM, M13, and Pf1 phage. The number of phage bound on the membrane increased with the offered concentration of phage and with time for each phage series.

In all experiments, phage predominantly bound early after breakthrough of the fluid. Over half of bound phage bound to fibers within 100 sec, before the bulk flow rate had decreased by about 50% (Figure S-7a). After flow ceased, unbound phage exhibited Brownian motion from which their diffusivity could be calculated from the mean-square displacement (Figure

S-7b). Because the flow rate was related to phage flux, we counted the flowing phage in the field of view at 20, 60, 100, 140, 180, 220, 260, 300, and 340 sec (Figure S-8a, b, and c) by subtracting the number of bound phage from the total number of phage in the field of view. The number of flowing phage in the membrane was nearly constant over time (Figure S-8a, b, and c), as the relatively large pore diameter (9 μm) did not hinder phage transport. The flux of phage through a fixed field of view decreased over time (Figure S-8d, e, and f). Because the number of flowing phage was constant, the decrease in flux reflected a decrease in the flow velocity (Figure S-7a) and capillary flow rate. The rate at which phage bound to the fiber network, calculated from the instantaneous derivative of the curves in Figure 3, was proportional to phage flux (Figure 4). This result suggested that increasing the chance that phage encounter fibers (by increasing their flux) promoted binding.

The three phage have different widths and lengths (Table 1). Because we varied both the dimensions and concentration of phage, we examined the dependence of binding on several metrics related to phage morphology, including total volume, surface area, and swept volume (per unit volume of solution). To calculate the total volume and surface area of phage, we approximated phage as cylinders of volume $\pi r^2 l$ and surface area $2\pi rl$, where r and l are radius and length of the phage, respectively, and multiplied by the phage concentration. To calculate the total swept volume, we calculated the volume of the sphere that would be created by a phage rotating in all three dimensions around its center of mass (swept volume = $(4/3)\pi l^3$) and multiplied by the phage concentration. The total number of bound phage from a 25 μl solution is shown as a function of number, total volume, total surface area, and total swept volume of phage in Figure 5a, b, c, and d, respectively. Generally, the number of bound phage increased with each metric. At a fixed concentration of $\frac{1}{16} \times 10^8$ pfu m^{-1}, for example, the number of bound Pf1 (longest) phage was greater than that of PVM (shortest) phage (Figure 5a). The total volume occupied by phage (Figure 5b) did not collapse all the binding curves, suggesting that binding was not controlled by crowding. Similarly, the total spherical volume swept out by phage as they flowed through the membrane (Figure 5d) did not collapse the binding curves, suggesting that phage did not tumble in flow. Instead, the number of bound phage collapsed for all three phage onto a single curve as a function of the total surface area (Figure 5c). These results indicated that the binding efficiency was related to phage surface area, not volume or swept volume. The surface area of phage increased linearly with the number of capsid proteins (CPs): ~1,600 CP for PVM,[31] ~2,800 CP for M13,[35] and ~7,000 CP for Pf1[36] ($R^2 = 0.987$), but not length because of the variation in diameters; hence the number of bound phage also collapsed for all phage onto a single curve as a function of the number of capsid proteins (Figure S-9). This result suggests that a similar fraction of capsid proteins bore biotins or that the biotin density was sufficient for efficient capture. The larger surface area (and hence number of capsid proteins) of the elongated phage increased the probability of interaction between phage and fibers in the membrane, suggesting that binding efficiency should increase with aspect ratio for phage reporters of fixed volume.

Surprisingly, the total swept volume did not correlate with the binding efficiency of phage, implying that phage do not rotate during flow. To test this idea, we used Jeffery orbit theory to evaluate the period of rotation of each phage in a steady linear flow field,[6] valid for a

ellipsoidal particle in an infinite fluid for which Brownian motion can be neglected. We first confirmed that our system approximately satisfied the two Jeffery orbit conditions: that (1) the flow was laminar and steady, and (2) advective transport dominated over diffusivity. Given the open pore network, we estimated the Reynolds number as Re = $\rho DV/\mu$, where ρ = 1,094 kg m^{-3} was the background solution density, D was the average fiber diameter, V was the phage velocity as a function of time (Figure S-7a), and μ = 8.67 cP was the solution viscosity measured at a fixed shear rate of 42 s^{-1} using an Ubbelohde viscometer. Similarly, we estimated the Péclet number as Pe = VD/D_p, where D_p = 0.134 μm^2 s^{-1} was the measured translational diffusivity of the Biotin-FluorM13 (Figure S-7b). At all times Re ≪ 1 (Table 2), confirming that the flow was laminar and steady, and Pe ≫ 1, confirming that Brownian motion could be neglected. Finally, phage were rodlike with high aspect ratios and could be approximated as ellipsoids. We therefore applied Jeffery orbit theory to calculate the phage tumbling period, $T=\frac{2\pi}{\dot{\gamma}}(r+1/r)$, where $\dot{\gamma}$ was the average shear rate (calculated by dividing the flow rate by the pore diameter) and r was the phage aspect ratio. The tumbling period increased with phage length (Table 2). Although PVM (the lowest aspect ratio phage studied) had a shorter tumbling period than M13 or Pf1, in most cases phage did not tumble as they passed through the field of view, unless tumbling was promoted by vorticity near fibers.[30] We therefore concluded that the swept volume did not control the binding efficiency in our system.

Effect of local flow conditions on phage binding

We hypothesized that the local flow near/on the fiber surfaces controlled binding of phage. Hence we identified the location of fibers in the fluorescence movies by acquiring brightfield images in the same focal area. Next, the flow profile was extracted across the entire fiber area and the speed and direction of the local flow were obtained at the positions where phage bound. These comparisons allowed us to relate the magnitude and direction of the local flow to the likelihood that phage bound there.

The speed and direction of the local flow at the locations of bound phage varied with time (Figure S-10), reflecting the decrease in capillary flow rate over time. To determine the effect of the local flow speed, we first normalized the flow speed by the difference between the local minimum and maximum speed for each PIV result (at 20, 60, 100, 140, 180, 220, 260, 300, and 340 sec after breakthrough) and then calculated the average local flow speed across the entire fiber area. Finally, we identified domains in which the local flow speed was slower and faster than the average local flow speed. Distributions of the number of bound phage as a function of the local flow speed are shown in Figure S-11. Each type of phage (PVM, M13, Pf1) bound in greater numbers in the faster local flow domain than in the slower domain, and more so as the aspect ratio increased (Figure 6). The result that phage were more likely to bind in the faster local flow domain is consistent with the idea that higher phage flux promotes binding, as suggested by the bulk flow studies (Figure 4).

Similarly, we compared the likelihood of binding to the angle at which the local flow encountered the fiber (Figure S-11). Here, we surmised that vorticity generated by flow near the fiber surface might reorient the phage and hence influence their binding interaction. In

contrast to the results for local velocity, however, phage did not exhibit a preferred local flow direction for binding (Figure S-12). Instead, the distribution of local flow angles across the bound phage population was constant within the error of the measurements. This omnidirectional binding likely arises from the large number of potential bonding interactions offered by the biotins attached to the phage major coat proteins.[30] Phage approaching the fiber could be captured on any of the biotins, thereby diminishing the dependence on orientation.

Conclusions

We investigated the effect of two assay parameters (phage flux and size) on the binding efficiency of phage reporters in fibrous glass LFA membranes. Filamentous phage of different lengths and widths were functionalized with biotin and AlexaFluor 555 on their coat proteins. Fusion 5 LFA strips were functionalized with NeutrAvidin. The number of phage bound to the fibers in the membrane was counted as a function of time in movies recorded during capillary flow. The rate at which phage bound correlated with their bulk flux through the membrane. At the local (pore) scale, phage were more likely to bind in regions within the membrane with faster local flow (and hence higher local flux). The number of bound phage also increased with phage length and aspect ratio. The capture cross-section controlling the binding efficiency was highly correlated with the phage surface area (but not with total phage volume, concentration, or swept volume) and with the number of capsid proteins, consistent with the idea that increasing the average bulk flux increased the likelihood that phage encountered a fiber.

Our results suggest that increasing the flux of phage increases the binding efficiency of elongated reporters in fibrous membranes. In turn, this suggests that careful tuning of membrane design variables such as the pore diameter and membrane geometry (which control the local and bulk flow rates) could increase binding efficiency and thus the sensitivity of LFAs. Similarly, increasing the surface area of reporters increases their binding efficiency, relative to a spherical particle of the same volume, by increasing the capture cross-section. This result suggests that using reporters of other shapes could be an effective and simple way to increase the analytical sensitivity of this important class of point-of-care diagnostics. More broadly, our understanding of how reporter flux and size affect capture and binding at the pore-scale may prove useful towards optimizing particle capture in a variety of microscale open porous media for applications in on-chip chromatography, virus purification, membrane chromatography, and microfluidic nanocomposite fabrication.

Supplementary Material

Refer to Web version on PubMed Central for supplementary material.

Acknowledgments

We acknowledge support from the NIAID (1R21AI111120-01A1, to RCW, JCC, and KK), the National Science Foundation (CBET-1511789, to JCC and RCW), and the Welch Foundation (E-1869, to JCC). We thank Ainars Leonchiks from ASLA Biotech for the generous gift of phage, and Maxwell Smith and Michael Byington for assistance in characterizing the pore and pore throat diameters of the Fusion 5 membranes.

References

1. Gubala V, Harris LF, Ricco AJ, Tan MX, Williams DE. Point of Care Diagnostics: Status and Future. Anal Chem. 2012; 84:487–515. [PubMed: 22221172]
2. Posthuma-Trumpie GA, Korf J, van Amerongen A. Lateral Flow (Immuno) Assay: Its Strengths, Weaknesses, Opportunities and Threats. A Literature Survey. Anal Bioanal Chem. 2009; 393:569–582. [PubMed: 18696055]
3. Lee S, Mehta S, Erickson D. Two-Color Lateral Flow Assay for Multiplex Detection of Causative Agents Behind Acute Febrile Illnesses. Anal Chem. 2016; 88:8359–8363. [PubMed: 27490379]
4. Choi JR, Hu J, Feng SS, Abas WAW, Pingguan-Murphy B, Xu F. Sensitive Biomolecule Detection in Lateral Flow Assay with a Portable Temperature-Humidity Control Device. Biosens Bioelectron. 2016; 79:98–107. [PubMed: 26700582]
5. Tang R, Yang H, Choi JR, Gong Y, Hu J, Feng S, Pingguan-Murphy B, Mei Q, Xu F. Improved Sensitivity of Lateral Flow Assay Using Paper-Based Sample Concentration Technique. Talanta. 2016; 152:269–276. [PubMed: 26992520]
6. Rohrman BA, Leautaud V, Molyneux E, Richards-Kortum RR. A Lateral Flow Assay for Quantitative Detection of Amplified HIV-1 RNA. PLoS One. 2012; 7
7. Liu BH, Tsao ZJ, Wang JJ, Yu FY. Development of a Monoclonal Antibody Against Ochratoxin A and its Application in Enzyme-Linked Immunosorbent Assay and Gold Nanoparticle Immunochromatographic Strip. Anal Chem. 2008; 80:7029–7035. [PubMed: 18698802]
8. Zhao Y, Wang HR, Zhang PP, Sun CY, Wang XC, Wang XR, Yang RF, Wang CB, Zhou L. Rapid Multiplex Detection of 10 Foodborne Pathogens with an Up-Converting Phosphor Technology-Based 10-Channel Lateral Flow Assay. Sci Rep. 2016; 6
9. Song C, Li J, Liu J, Liu Q. Simple Sensitive Rapid Detection of Escherichia coli O157:H7 in Food Samples by Label-Free Immunofluorescence Strip Sensor. Talanta. 2016; 156-157:42–7. [PubMed: 27260433]
10. Fenton EM, Mascarenas MR, López GP, Sibbett SS. Multiple Lateral-Flow Test Strips Fabricated by Two-Dimensional Shaping. ACS Appl Mater Interfaces. 2009; 1:124–129. [PubMed: 20355763]
11. Parolo C, Medina-Sanchez M, de la Escosura-Muniz A, Merkoçi A. Simple Paper Architecture Modifications Lead to Enhanced Sensitivity in Nanoparticle Based Lateral Flow Immunoassays. Lab Chip. 2013; 13:386–390. [PubMed: 23223959]
12. Paterson AS, Raja B, Garvey G, Kolhatkar A, Hagström AEV, Kourentzi K, Lee TR, Willson RC. Persistent Luminescence Strontium Aluminate Nanoparticles as Reporters in Lateral Flow Assays. Anal Chem. 2014; 86:9481–9488. [PubMed: 25247754]
13. Bruno JG. Application of DNA Aptamers and Quantum Dots to Lateral Flow Test Strips for Detection of Foodborne Pathogens with Improved Sensitivity versus Colloidal Gold. Pathogens. 2014; 3:341–55. [PubMed: 25437803]
14. Barnett JM, Wraith P, Kiely J, Persad R, Hurley K, Hawkins P, Luxton R. An Inexpensive, Fast and Sensitive Quantitative Lateral Flow Magneto-Immunoassay for Total Prostate Specific Antigen. Biosensors. 2014; 4:204–20. [PubMed: 25587419]
15. Swanson C, D'Andrea A. Lateral Flow Assay with Near-Infrared Dye for Multiplex Detection. Clin Chem. 2013; 59:641–648. [PubMed: 23364182]
16. Huang M, Galarreta BC, Cetin AE, Altug H. Actively Transporting Virus Like Analytes with Optofluidics for Rapid and Ultrasensitive Biodetection. Lab Chip. 2013; 13:4841–4847. [PubMed: 24170146]
17. Chang KC, Hammer DA. The Forward Rate of Binding of Surface-Tethered Reactants: Effect of Relative Motion Between Two Surfaces. Biophys J. 1999; 76:1280–1292. [PubMed: 10049312]
18. Hansen R, Bruus H, Callisen TH, Hassager O. Transient Convection, Diffusion, and Adsorption in Surface-Based Biosensors. Langmuir. 2012; 28:7557–7563. [PubMed: 22509887]
19. Squires TM, Messinger RJ, Manalis SR. Making it stick: convection, reaction and diffusion in surface-based biosensors. Nat Biotechnol. 2008; 26:417–426. [PubMed: 18392027]
20. Berli CLA, Kler PA. A Quantitative Model for Lateral Flow Assays. Microfluid Nanofluid. 2016; 20:104.

21. Sajid M, Kawde AN, Daud M. Designs, Formats and Applications of Lateral Flow Assay: A Literature Review. J Saudi Chem Soc. 2015; 19:689–705.
22. Fullstone G, Wood J, Holcombe M, Battaglia G. Modelling the Transport of Nanoparticles under Blood Flow using an Agent-based Approach. Sci Rep. 2015; 5
23. Decuzzi P, Ferrari M. The Adhesive Strength of Non-Spherical Particles Mediated by Specific Interactions. Biomaterials. 2006; 27:5307–5314. [PubMed: 16797691]
24. Tan JF, Shah S, Thomas A, Ou-Yang HD, Liu YL. The Influence of Size, Shape and Vessel Geometry on Nanoparticle Distribution. Microfluid Nanofluid. 2013; 14:77–87. [PubMed: 23554583]
25. Xu H, Chen J, Birrenkott J, Zhao JX, Takalkar S, Baryeh K, Liu GD. Gold-Nanoparticle-Decorated Silica Nanorods for Sensitive Visual Detection of Proteins. Anal Chem. 2014; 86:7351–7359. [PubMed: 25019416]
26. Jana NR. Nanorod Shape Separation using Surfactant Assisted Self-Assembly. Chem Commun. 2003:1950–1951.
27. Adhikari M, Dhamane S, Hagström AEV, Garvey G, Chen W, Kourentzi K, Strych U, Willson RC. Functionalized Viral Nanoparticles as Ultrasensitive Reporters in Lateral-Flow Assays. Analyst. 2013; 138:5584–5587. [PubMed: 23905160]
28. Kim J, Adhikari M, Dhamane S, Hagström AEV, Kourentzi K, Strych U, Willson RC, Conrad JC. Detection of Viruses By Counting Single Fluorescent Genetically Biotinylated Reporter Immunophage Using a Lateral Flow Assay. ACS Appl Mater Interfaces. 2015; 7:2891–2898. [PubMed: 25581289]
29. Adhikari M, Strych U, Kim J, Goux H, Dhamane S, Poongavanam MV, Hagström AEV, Kourentzi K, Conrad JC, Willson RC. Aptamer-Phage Reporters for Ultrasensitive Lateral Flow Assays. Anal Chem. 2015; 87:11660–11665. [PubMed: 26456715]
30. Kim J, Poling-Skutvik R, Trabuco JRC, Kourentzi K, Willson RC, Conrad JC. Orientational Binding Modes of Reporters in a Viral-Nanoparticle Lateral Flow Assay. Analyst. 2017; 142:55–64.
31. Kalnciema I, Balke I, Skrastina D, Ose V, Zeltins A. Potato Virus M-Like Nanoparticles: Construction and Characterization. Mol Biotechnol. 2015; 57:982–992. [PubMed: 26346833]
32. Washburn EW. The Dynamics of Capillary Flow. Phys Rev. 1921; 17:273–283.
33. Willert CE, Gharib M. Digital Particle Image Velocimetry. Exp Fluids. 1991; 10:181–193.
34. JPIV. http://www.jpiv.vennemann-online.de/ (accessed July 11th 2016).
35. Stopar D, Spruijt RB, Wolfs C, Hemminga MA. Protein-Lipid Interactions of Bacteriophage M13 Major Coat Protein. Biochim Biophys Acta, Biomembr. 2003; 1611:5–15.
36. Thiriot DS, Nevzorov AA, Opella SJ. Structural Basis of the Temperature Transition of Pf1 Bacteriophage. Protein Sci. 2005; 14:1064–1070. [PubMed: 15741342]

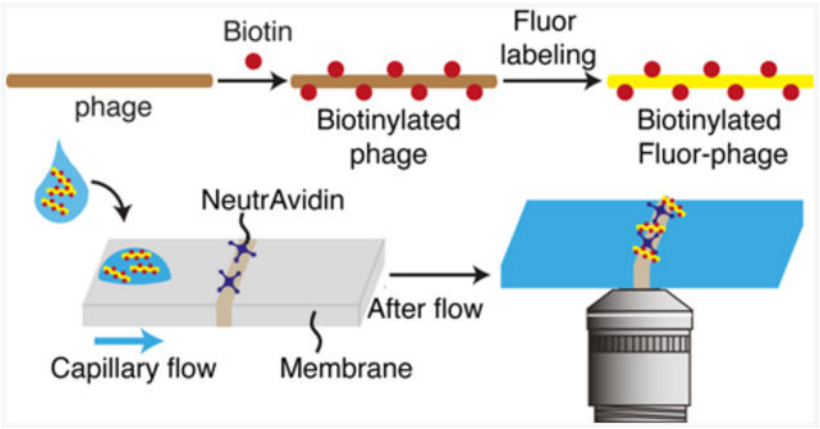

Figure 1. Schematic of phage modification and capture

Phage were labeled with biotin and AlexaFluor 555 dyes on the major coat protein. Biotinylated Fluor-phage were detectable by epi-fluorescence microscopy and capturable by NeutrAvidin immobilized on a glass fibrous membrane.

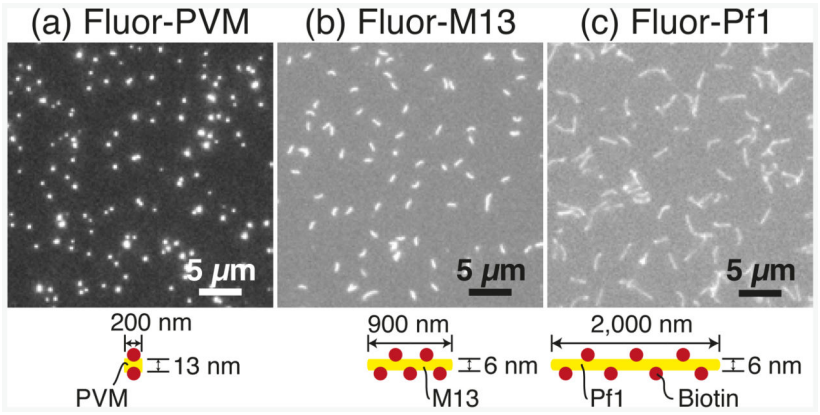

Figure 2. Phage reporter series

Bacteriophage (a) PVM (length 200 nm and width 13 nm), (b) M13 (length 900 nm and width 6 nm), or (c) Pf1 (length 2,000 nm and width 6 nm) were covalently modified with biotin and AlexaFluor 555 on their major coat proteins. The aspect ratios of PVM, M13, and Pf1 are 15, 150, and 333, respectively.

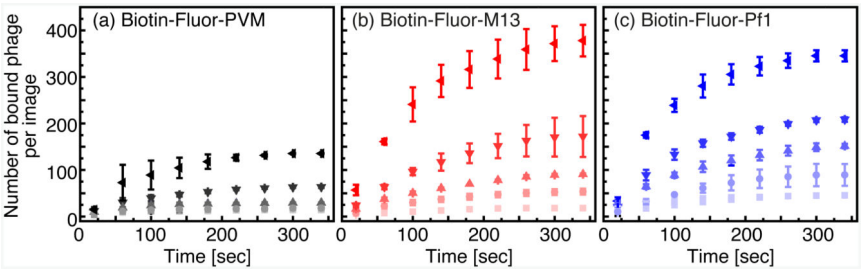

Figure 3. Bound phage counting results

Number of bound (a) PVM, (b) M13, or (c) Pf1 phage at the NeutrAvidin line in Fusion 5 membranes as a function of time. Symbols indicate the concentration of phage in a two-fold dilution series: [$\frac{1}{2} \times 10^8$ (◄), $\frac{1}{4} \times 10^8$ (▼), $\frac{1}{8} \times 10^8$ (▲), $\frac{1}{16} \times 10^8$ (●), **and** $\frac{1}{32} \times 10^8$ (■) pfu ml^{-1}]. The number of bound phage depended on concentration and time. Error bars indicate the standard deviation measured from three independent experiments in different Fusion 5 membranes for each phage type and concentration.

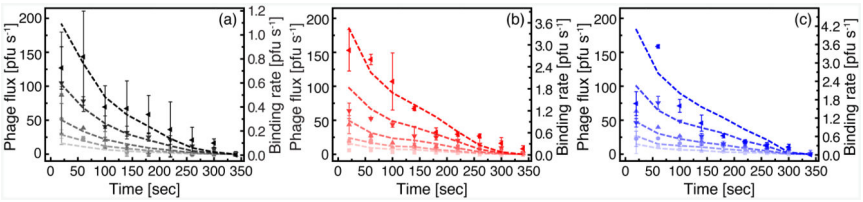

Figure 4. Comparison of binding rate with phage flux

The binding rate (symbols) of phage (a) PVM, (b) M13, or (c) Pf1 phage calculated from Figure 3 was compared with phage flux (dashed lines, Figure S8d – f). Symbols indicated the binding rate at the concentration of phage in a twofold dilution series: [$\frac{1}{2} \times 10^8$ (◄), $\frac{1}{4} \times 10^8$ (▼), $\frac{1}{8} \times 10^8$ (▲), $\frac{1}{16} \times 10^8$ (●), and $\frac{1}{32} \times 10^8$ (■) pfu ml^{-1}]. The color of the dashed line indicates the phage flux at each concentration. Error bars indicate the standard deviation measured from three independent experiments in different Fusion 5 membranes for each phage type and concentration.

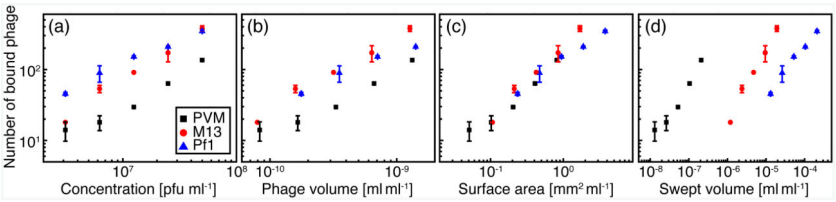

Figure 5. Number of bound phage as function of (a) phage concentration, (b) total phage volume, (c) total phage surface area, and (d) total phage swept volume (per unit volume of solution)

The collapse of all curves to a common trend in (c) indicates that the surface area of phage controls their binding efficiency. Error bars indicate the standard deviation measured from three independent experiments in different Fusion 5 membranes for each phage type and concentration.

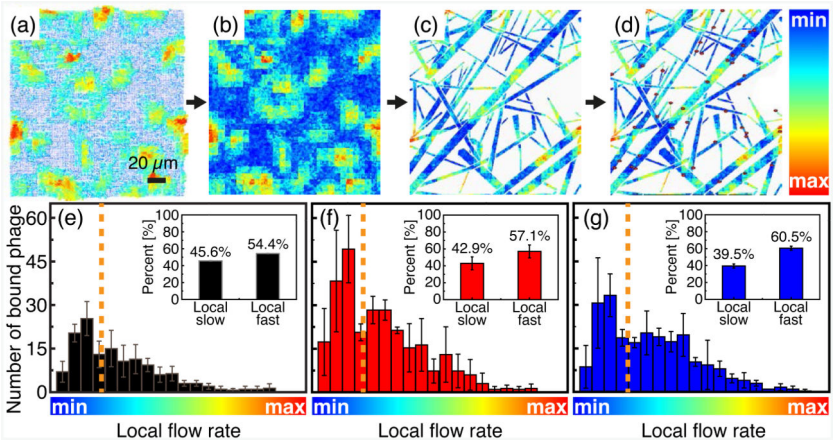

Figure 6. Binding efficiency depends on local flow rate

(a) PIV analysis and the (b) extracted flow speeds. (c) Flow speeds at the positions of the fibers, with (d) positions where individual phage bound overlaid (as ovals). The average local flow rate (vertical dashed lines in e, f, g) was calculated across the entire fiber. Slower and faster flow domains featured local flow rates that were slower and faster, respectively, than the average local flow rate. Phage binding only occurred on the fiber surface. (e) – (g) Number of bound phage as a function of local velocity for (e) PVM, (f) M13, and (g) Pf1. The orange vertical dashed lines indicate the boundaries between slower and faster local flow domains. For each phage type, a greater number of phage bound in the faster local flow domain than in the slower domain. Insets to (e) – (g): Percent of phage binding in slower and faster domains. Error bars indicate the standard deviation measured from three independent experiments in different Fusion 5 membranes.

Table 1

Phage dimensions and relative volume, surface area, and swept volume

Phage	Diameter (nm)	Length (nm)	Relative volume *	Relative surface area **	Relative swept volume ***
PVM	13	200	1	1	1
M13	6	900	0.96	2.1	91
Pf1	6	2,000	2.1	4.6	1000

* Relative volume: Phage were approximated as cylinders of radius r and length l, so that the volume was calculated as $\pi r^2 l$. The PVM volume was chosen as the reference volume for relative comparisons.

** Relative surface area: The surface area was calculated as $2\pi rl$. The PVM surface area was chosen as the reference surface area for relative comparisons.

*** Relative swept volume: The swept volume, the volume of the sphere swept out when phage rotated in all three dimensions, was calculated as $4\pi l^3/3$. The PVM swept volume was chosen as the reference swept volume for relative comparisons.

Table 2

Péclet and Reynolds numbers, and corresponding tumbling period of phage as a function of time

Time (sec)	Reynolds number	Péclet number (for M13 phage)	Tumbling period (sec)		
			PVM	M13	Pf1
20	1.7×10^{-4}	1.0×10^{4}	3.2	33	72
100	8.8×10^{-5}	5.0×10^{3}	6.6	63	143
180	5.1×10^{-5}	3.0×10^{3}	13	97	238
260	1.5×10^{-5}	9.1×10^{2}	53	388	575